Research Article | Vol. 31, No. 17 / 14 Aug 2023 / Optics Express 27830
Optics EXPRESS

Self-calibrated NICE-OHMS based on an asymmetric signal: theoretical analysis and experimental validation

YUETING ZHOU,[1,2] ZIHAO ZHANG,[1,2] YANKE LI,[1,2] GANG ZHAO,[1,2,5] XIAOBIN ZHOU,[1,2] BOFENG ZHANG,[1,2] KANG JIAO,[1,2] XIAOJUAN YAN,[1,2] CHUANLIANG LI,[3] OVE AXNER,[4] AND WEIGUANG MA[1,2,6]

[1]*State Key Laboratory of Quantum Optics & Quantum Optics Devices, Institute of Laser Spectroscopy, Shanxi University, 030006 Taiyuan, China*
[2]*Collaborative Innovation Center of Extreme Optics, Shanxi University, 030006 Taiyuan, China*
[3]*School of Applied Science, Taiyuan University of Science and Technology, 030024 Taiyuan, China*
[4]*Department of Physics, Umeå University, Umeå, SE-90187, Sweden*
[5]*gangzhao@sxu.edu.cn*
[6]*mwg@sxu.edu.cn*

Abstract: As an ultra-sensitive detection technique, the noise-immune cavity enhanced optical heterodyne molecular spectroscopy (NICE-OHMS) technique has great potential for assessment of the concentration of trace gases. To determine gas concentrations at the ppt or lower level with high accuracy, it is desirable that the technique exhibits self-calibration (or calibration-free) capabilities. Although being sensitive, NICE-OHMS has so far not demonstrated any such ability. To remedy this, this paper provides a self-calibrated realization of NICE-OHMS that is based on a switching of the feedback target of the DeVoe-Brewer (DVB) locking procedure from the modulation frequency of the frequency modulation spectroscopy (FMS) to the cavity length, which creates an asymmetrical signal whose form and size can be used to unambiguously assess the gas concentration. A comprehensive theoretical model for self-calibrated NICE-OHMS is established by analyzing the shift of cavity modes caused by intracavity absorption, demonstrating that gas absorption information can be encoded in both the laser frequency and the NICE-OHMS signal. To experimentally verify the methodology, we measure a series of dispersion signals under different levels of absorbance using a built experimental setup. An instrument factor and the partial pressure are obtained by fitting the measured signal through theoretical expressions. Our results demonstrate that fitted values are more accurate for higher partial pressures than for lower. To improve on the accuracy at low partial pressures, it is shown that the instrument factor obtained by fitting the signal at large partial pressures (in this case, above 7.8 μTorr) can be set to a fixed value for all fits. By this, the partial pressures can be assessed with a relative error below 0.65%. This technique has the potential to enable calibration-free ultra-sensitive gas detection.

1. Introduction

Laser absorption spectroscopy (LAS) has the advantages of being highly sensitivity and provide non-invasive, in-situ, and real time assessments for atomic or molecular analysis. It has been widely demonstrated that it constitutes a useful tool for trace gas detection [1–6] as well as fundament researches, such as test of basic physical laws [7]. Sensitivity, which determines the minimal detectable gas concentration (MDC), is one of the most key performance factors of LAS. To improve on it, various strategies have been proposed. For example, to mitigate low frequency noise, modulation techniques have been introduced, leading to the development of techniques such as wavelength modulation spectroscopy (WMS) [8] and frequency modulation

#497862 https://doi.org/10.1364/OE.497862
Journal © 2023 Received 13 Jun 2023; revised 26 Jul 2023; accepted 26 Jul 2023; published 4 Aug 2023

Optics EXPRESS

spectroscopy (FMS) [9]. To enhance the absorption signal by increasing the interaction length between laser and target gas, multipass cells or resonant cavities have been utilized. However, the number of laser reflections by an optical cavity could be above 10^4, which is almost two or three orders of magnitude higher than that by a multi-pass cell. This has led to the development of techniques, such as optical feedback cavity enhanced absorption spectroscopy (OF-CEAS) [10,11], cavity ringdown spectroscopy (CRDS) [12], and off axis integrated cavity output spectroscopy (OA-ICOS) [13,14]. Another method is to combine modulation and cavity-based techniques. Using this concept, noise-immune cavity enhanced optical heterodyne molecular spectroscopy (NICE-OHMS), which is based on a combination of FMS and CEAS, has been developed [15]. Thanks to its immunity to frequency-to-amplitude noise, NICE-OHMS constitutes the most sensitive LAS technique. A shot noise limited response and sensitivity down to $10^{-14}\,\mathrm{cm}^{-1}$ level has been achieved [16,17].

This is why direct absorption spectroscopy (DAS) and CRDS are preferred, as they enable the deduction of absolute gas concentration according to Beer-Lambert Law or the variation of the ringdown time [12]. However, for modulation techniques, instrumental factors are additionally introduced by the demodulation process, which can complicate the accurate evaluation of concentrations. As a result, techniques, such as WMS, FMS and NICE-OHMS, require in general calibration with reference gases of known concentrations. For WMS, the $1f$ normalized $2f$ signal can measure the gas concentration without regular calibration by eliminating the instrumental factor [18].

Whether regular calibration is required or not is another important factor to consider for the application of LAS, especially in scenarios that require independent measurements. To determine gas sample concentrations at the ppt or lower level, which, for example, is needed for traceable quantification of radiocarbon ^{14}C emission, it is desirable (or maybe even imperative) that NICE-OHMS has a self-calibration or calibration-free capability. In this paper, we define "self-calibration (or calibration-free)" as a method that does not rely on external intervention, such as using reference gases of known concentrations, to calibrate the signal regularly. As a step towards this, in 2010, Schmidt et al. presented an alternative mode of operation of NICE-OHMS. They tracked the frequency shifts of the free spectral range (FSR) of the cavity when performing the Pound-Drever-Hall (PDH) and DeVoe-Brewer (DVB) lockings [19]. The error signal of the DVB locking, which controls the modulation frequency, provides information about the FSR, which, in turn, could be used to assess gas concentration. However, since the immunity to frequency-to-amplitude noise is lost, the signal to noise ratio (SNR) of their signal was lower than that of conventional NICE-OHMS. This pioneering work could therefore not fully combine the high detection sensitivity of NICE-OHMS with calibration-free detection.

Based on the consideration of improving the long-term stability of NICE-OHMS signal, we improved the optical frequency accuracy by implementing feedback control of the cavity length instead of the FMS modulation frequency for DVB locking. In this process, the cavity length was stabilized to an RF signal while the laser frequency was locked to the cavity length. As a result, a stable and linearly tunable optical frequency was generated with linear tuning of the FMS modulation frequency when there is no gas inside the cavity [20]. When there is gas inside the cavity, we discovered that, with linear tuning of the FMS modulation frequency, the intracavity dispersion would lead to a non-linear response of the laser frequency. The demodulated NICE-OHMS signal would then exhibit an unusual and asymmetrical profile, with the degree of asymmetry increasing with greater gas dispersion. This implies that the amount of asymmetry of the NICE-OHMS profile could include information about the gas concentration, thus providing an opportunity to give the technique a self-calibration ability for trace gas detection. This finding is the basis for the novel self-calibrated NICE-OHMS methodology that is presented in this work.

Optics EXPRESS

The paper is organized as follows. Firstly, following the process used to deduce the full theoretical description of conventional NICE-OHMS by our group [21], a theoretical model for this new self-calibrated NICE-OHMS methodology is provided. In this, the relationship between the NICE-OHMS signal, the cavity FSR, and the gas dispersion is established, by which the self-calibration property is analyzed. Finally, an experimental verification is conducted by measuring Doppler broadened dispersion NICE-OHMS signals of acetylene in the 1531 nm wavelength range.

2. Theoretical description of self-calibrated NICE-OHMS

2.1. Principle overview

Figure 1 displays a schematic diagram of the self-calibrated NICE-OHMS scheme, which employs two simultaneously applied locking techniques (PDH and DVB). To accomplish this, two distinct RF frequencies, ν_{PDH} and ν_m, are used to modulate the laser as it passes through an electro-optic modulator (EOM). The ν_{PDH} should be significantly larger than the cavity mode linewidth but smaller than the cavity FSR and is typically in the MHz range, while ν_m is in the order of the cavity FSR (500 MHz for a 30 cm long cavity). The two error signals for the two frequency lockings are derived from the demodulation of the cavity reflection at the ν_{PDH} and ν_m-ν_{PDH} frequencies, respectively.

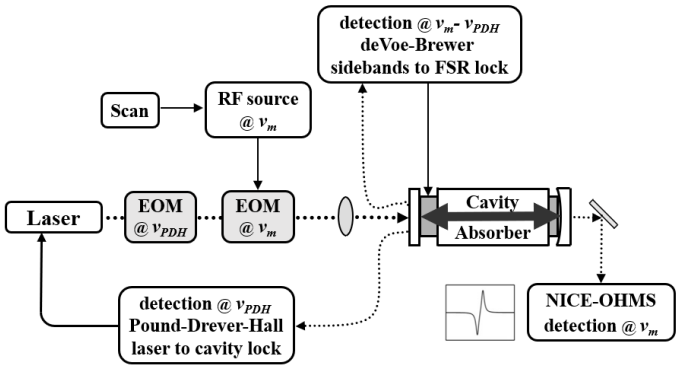

Fig. 1. Schematic illustration of self-calibrated NICE-OHMS.

The laser carrier is secured to the center cavity mode by use of the PDH locking. In contrast to conventional NICE-OHMS, the feedback of the DVB error signal is sent to the cavity length, ensuring that both the cavity FSR and the laser frequency are linked to ν_m. Hence, when the ν_m is scanned, both the cavity length and the laser frequency are automatically scanned.

When there is gas inside the cavity, the cavity modes near the absorption line are no longer evenly spaced due to the dispersion of the gas, which is associated with its absorption by the Kramers-Kronig relations [22,23]. When scanning the modulation frequency ν_{m}, this will give rise to a nonlinear change of the cavity length, and thereby non-linear alterations in both the laser frequency and the FSR. Demodulating the cavity transmission signal at ν_{m} will thereby provide a NICE-OHMS signal that is distorted due to the nonlinear response of the laser frequency. The stronger the intracavity absorption, the more prominent the distortion will be. Such signal and laser frequency distortions can be theoretically modelled and provide the basis for the calibration-free property of the technique when gas concentrations are addressed. A detailed theoretical description is provided below, with most of the notations as defined in [21]. For the completeness of the theory, part of previous descriptions is repeated.

Optics EXPRESS

2.2. FSR, optical frequency, and relative frequency detunings under dual frequency locking conditions

2.2.1. Simplified description – modulation of the light with a small modulation index creating one pair of sidebands

The principle of self-calibrated NICE-OHMS is displayed in Fig. 2 for the case when the modulation of the light is done with a small modulation index creating solely one pair of sidebands. Panel (a) describes three cavity modes with center frequencies of $(q\text{-}1)\nu_{FSR}^0$, $q\nu_{FSR}^0$, and $(q+1)\nu_{FSR}^0$, where ν_{FSR}^0, defined as c/(2L_0), is the FSR of the empty cavity, q is the mode number and L_0 is the cavity length, together with a dual modulated laser whose modulation frequencies are ν_{PDH} and ν_m. The ν_{PDH} is used to enable the laser frequency, ν_0^l, to be linked to the cavity mode, $q\nu_{FSR}^0$, while the ν_m is used to perform the FMS and to produce, in combination with ν_{PDH}, the error signal of the DVB locking. The ν_m is generated by an RF source as a reference that constitutes a multiple of the cavity FSR, $n\nu_{FSR}^0$, locked by the DVB technique. The status of the frequency locking without analyte, achieved by use of the PDH and the DVB techniques, i.e. $\nu_0^l = q\nu_{FSR}^0$ and $\nu_{FSR}^0 = \nu_m$, is shown in panel (a) in Fig. 2.

Figure 2(b) displays the variation of the refractive index caused by the presence of an absorber with a center frequency of ν_0^a. Let us denote the change of refractive index at the $(q+n)^{th}$ cavity mode caused by the gas absorption at the center frequency of the target transition ν_0^a by Δn_{q+n}^a, where n is the order of sideband (here 0 or ±1). As previously has been shown [15,19], Δn_{q+n}^a can be expressed as

$$\Delta n_{q+n}^a = \frac{\alpha_0 L_0}{2\pi}\frac{1}{q+n}\bar{\chi}_{q+n}^{a.disp} \tag{1}$$

where α_0 is the absorption coefficient represented by the product of the line strength, the pressure, the concentration, and the absorption lineshape function, L_0 is the empty cavity length, while $\bar{\chi}_{q+n}^{a.disp}$ represents the dispersion part of the peak normalized absorption lineshape function. The absorption lineshape function is a Voigt function, which is suitable for describing the broadening of spectral lines in a variety of conditions, including both low and high pressures.

Panel (c) displays the shifts of the cavity modes caused by the refractive index. According to the description in Ma et al. [20,21], the cavity modes will shift from $(q+n)\nu_{FSR}^0$ to $(q+n)\nu_{FSR}^0(1\text{-}\Delta n_{q+n}^a)$. The shifts of the mode frequencies, $\Delta\nu_{q+n}^{c,a}$, are thus equal to $\Delta n_{q+n}^a(q+n)\nu_{FSR}^0$. This implies that also the separation between adjacent cavity modes will shift. Since $\bar{\chi}_{q+n}^{a.disp}$ is frequency dependent, these separations will likewise be frequency dependent. Hence, in the presence of gas, the modulation frequency of the laser, ν_m, cannot fully match all cavity mode separations.

When the two frequency locking processes are activated, the locking conditions can be restated as follows [19,21,24,25].

$$S_{\nu_{PDH}} = \mathrm{Im}[J_0^2(\beta)\chi_q^{c,r,a}(\delta_0^a,\phi_0^a,\varphi_0^0) + J_1^2(\beta)[\chi_{q-1}^{c,r,a}(\delta_{-1}^a,\phi_{-1}^a,\varphi_{-1}^0) + \chi_{q+1}^{c,r,a}(\delta_1^a,\phi_1^a,\varphi_1^0)]] = 0 \tag{2}$$

$$S_{\nu_{DVB}} = \mathrm{Im}[\chi_{q-1}^{c,r,a}(\delta_{-1}^a,\phi_{-1}^a,\varphi_{-1}^0) - \chi_{q+1}^{c,r,a}(\delta_1^a,\phi_1^a,\varphi_1^0)] = 0 \tag{3}$$

where $\chi_{q+n}^{c,r,a}(\delta_n^a,\phi_n^a,\varphi_n^0)$, δ_n^a, ϕ_n^a and φ_n^0 are explicitly given in Ma et al. [21]. In contrast to the empty cavity situation, the cavity modes are not perfectly synchronized with their corresponding laser components, which is shown in panel (d).

In the self-calibrated NICE-OHMS scheme, the DVB error signal provides feedback to the cavity length, whose change is denoted ΔL. The cavity modes will shift from $(q+n)\nu_{FSR}^0(1\text{-}\Delta n_{q+n}^a)$ to $(q+n)\nu_{FSR}^{0,Lock}(1\text{-}\Delta n_{q+n}^a)$, where $\nu_{FSR}^{0,Lock}$ is the FSR with the refreshed cavity length under the DVB locking condition, defined as c/[2(L_0+ΔL)]. This implies that, during locking, and in the presence of an absorber, as is illustrated in panel (d), the relative frequency deviation of the lower

Optics EXPRESS

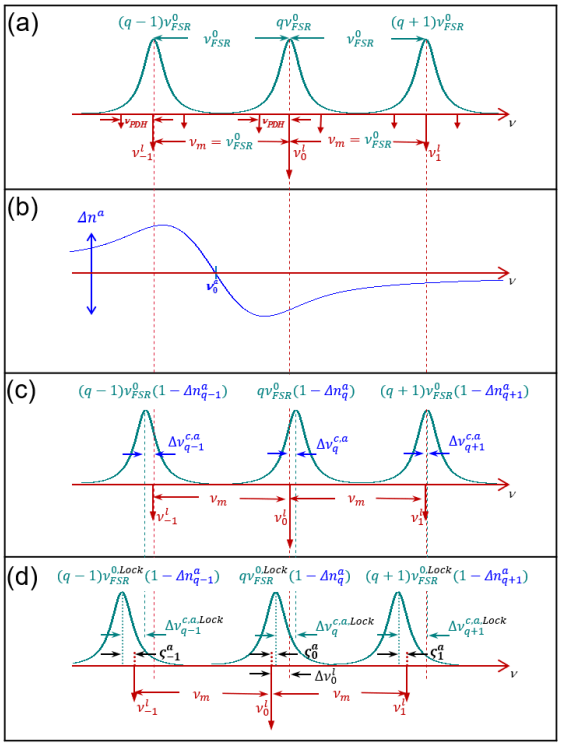

Fig. 2. Principle of self-calibrated NICE-OHMS based on the relationship between the cavity modes (green curves) and the laser frequency FMS components (red solid arrows), ν^l_n. Panel (a) displays the relationship for locking to an empty cavity. Panel (b) shows the index of refraction as a function of frequency for a target transition, ν^a_0. The panels (c) and (d) illustrate the corresponding relationships without and with locking for a cavity containing an absorber. $(q+n)\nu^0_{FSR}$, $(q+n)\nu^0_{FSR}(1\text{-}\Delta n^a_{q+n})$, and $(q+n)\nu^{0,Lock}_{FSR}(1\text{-}\Delta n^a_{q+n})$ are the center frequencies of the cavity modes corresponding to above three cases. $\Delta\nu^{c,a}_{q+n}$ and $\Delta\nu^{c,a,Lock}_{q+n}$ represent the shifts of the cavity modes in the absence and presence of locking. (For convenience of the description, the FMS components are considered to constitute a triplet, which is appropriate for a small modulation index.)

Optics EXPRESS

and upper laser sidebands from the corresponding cavity modes ς^a_{-1} and ς^a_1, can be expressed in terms of the relative frequency deviation of the carrier, ς^a_0, as

$$\begin{aligned}\varsigma^a_{-1} &= \varsigma^a_0 - \nu_m + \nu^{0,Lock}_{FSR} - \nu^{0,Lock}_{FSR}[q\Delta n^a_q - (q-1)\Delta n^a_{q-1}] \\ \varsigma^a_1 &= \varsigma^a_0 + \nu_m - \nu^{0,Lock}_{FSR} + \nu^{0,Lock}_{FSR}[(q+1)\Delta n^a_{q+1} - q\Delta n^a_q]\end{aligned} \tag{4}$$

where the relative frequency deviation of an individual mode, ς^a_n, can be expressed as $\varsigma^a_{0,\pm1} = \nu^l_{0,\pm1} - [q + (0,\pm1)]\nu^{0,Lock}_{FSR}(1 - \Delta n^a_{q+(0,\pm1)})$. Simultaneously, the laser frequency of the carrier can be expressed as

$$\nu^l_0 = \varsigma^a_0 + q\nu^{0,Lock}_{FSR}(1 - \Delta n^a_q) \tag{5}$$

This implies that, under locking conditions, the shift of the laser frequency (with and without the target gas in the cavity) can be expressed as $\Delta\nu^l_0 = \varsigma^a_0 + q\nu^{0,Lock}_{FSR}(1 - \Delta n^a_q) - q\nu_m$.

Since the two frequency lockings occur simultaneously, under the condition that the key experimental parameters ν_m, F, the modulation index β, q, and $\alpha_0 L_0$, and the expressions of $\chi^{c,r,a}_q$ and $\bar{\chi}^{a,disp}_n$ are known, the $\nu^{0,Lock}_{FSR}$, ν^l_0 and ς^a_n, upon which the expression for the NICE-OHMS signal is based (see below), can be obtained by solving the group of Eqs. (2)–(5).

2.2.2. Extended description – modulation of the light with an arbitrary modulation index creating a multitude of sidebands

It should be noted that the above analysis corresponds to the situation under which the modulation index for modulation frequency ν_m is significantly less than 1 (i.e., $\beta<<1$) for which the laser comprises a carrier and solely a single pair of side bands. However, since the NICE-OHMS signal amplitude depends on the β, it has been found that the optimum modulation indices do not adhere to this condition. In the Doppler limit and under unsaturation conditions, the optimum modulation indices are 1.55 and 1.2 for the absorption and dispersion detection phases, respectively [26,27]. Under these conditions, also higher order sidebands will contribute to the NICE-OHMS signal. The PDH and DVB locking conditions can then be written as:

$$\begin{aligned}S_{\nu_{PDH}} = \mathrm{Im}[&J^2_0(\beta)\chi^{c,r,a}_q(\delta^a_0, \phi^a_0, \varphi^0_0) \\ &+ \sum_{n=1}^{N} J^2_n(\beta)[\chi^{c,r,a}_{q-n-1}(\delta^a_{-n-1}, \phi^a_{-n-1}, \varphi^0_{-n-1}) + \chi^{c,r,a}_{q+n+1}(\delta^a_{n+1}, \phi^a_{n+1}, \varphi^0_{n+1})]] = 0\end{aligned} \tag{6}$$

$$S_{DVB} = \sum_{n=0}^{N} J_n(\beta)J_{n+1}(\beta)\mathrm{Im}\left[\begin{array}{c}\chi^{c,r,a}_{q-n-1}(\delta^a_{-n-1}, \phi^a_{-n-1}, \varphi^0_{-n-1}) - \chi^{c,r,a}_{q+n+1}(\delta^a_{n+1}, \phi^a_{n+1}, \varphi^0_{n+1}) \\ +\chi^{c,r,a}_{q-n}(\delta^a_{-n}, \phi^a_{-n}, \varphi^0_{-n}) - \chi^{c,r,a}_{q+n}(\delta^a_n, \phi^a_n, \varphi^0_n)\end{array}\right] = 0 \tag{7}$$

where the order of sideband, n, now can take several integer numbers. The relative frequency detunings can then be expressed as:

$$\begin{aligned}\varsigma^a_{-n} &= \varsigma^a_0 - n\nu_m + n\nu^{0,Lock}_{FSR} - \nu^{0,Lock}_{FSR}[q\Delta n^a_q - (q-n)\Delta n^a_{q-n}] \\ \varsigma^a_n &= \varsigma^a_0 + n\nu_m - n\nu^{0,Lock}_{FSR} + \nu^{0,Lock}_{FSR}[(q+n)\Delta n^a_{q+n} - q\Delta n^a_q]\end{aligned} \tag{8}$$

Similar to the situation with a small modulation index, by simultaneously resolving the group of Eqs. (5)–(8), the $\nu^{0,Lock}_{FSR}$, ν^l_0, and ς^a_n can be retrieved if the necessary key parameters are known.

2.3. NICE-OHMS signal

For most sensitive detection, the signal should be run under the conditions that gives the largest possible signal. Therefore, the self-calibrated NICE-OHMS methodology should be scrutinized

Optics EXPRESS

for the condition with arbitrarily large modulation index (as is given by the extended description in section 2.2.2 above). Under this condition, the Db NICE-OHMS signal can be described as [21,26]

$$S_{NO}(\Delta\nu_0^{l,a},\theta_{fm}) = \eta\sum_{n=0}^{N}\left(\begin{array}{l} J_n(\beta)J_{n+1}(\beta) \\ \left\{\begin{array}{l} [\Delta_{n+1}\Delta_n - \Delta_{-n-1}\Delta_{-n} - \Phi_{-n-1}\Phi_{-n} + \Phi_n\Phi_{n+1}]\sin\theta_{fm} \\ +[\Phi_{n+1}\Delta_n + \Delta_{-n}\Phi_{-n-1} - \Phi_{-n}\Delta_{-n-1} - \Phi_n\Delta_{n+1}]\cos\theta_{fm} \end{array}\right\} \end{array}\right) \quad (9)$$

where J_n, θ_{fm}, and η are Bessel functions of order n, the demodulation phase, and an instrument factor, respectively. $\Delta\nu_0^{l,a}$ is the laser frequency detuning, given by $\nu_0^l - \nu_0^a$. The $\Delta_{\pm n}$ and $\Phi_{\pm n}$ represent the real and imaginary parts of the complex transmission function through the cavity of the $\pm n^{th}$ laser components in the presence of gas, which, according to Ma et al. [21], can be written as

$$\begin{aligned} \Delta_{\pm n} &= (-1)^{q\pm n}\frac{1+\frac{2F}{\pi}r\delta_{\pm n}^a}{1+\frac{4F}{\pi}r\delta_{\pm n}^a+\left(\frac{2F}{\pi}\right)^2[(r\delta_{\pm n}^a)^2+(\psi_{\pm n}^a)^2]} \\ \Phi_{\pm n} &= (-1)^{q\pm n}\frac{\frac{2F}{\pi}\psi_{\pm n}^a}{1+\frac{4F}{\pi}r\delta_{\pm n}^a+\left(\frac{2F}{\pi}\right)^2[(r\delta_{\pm n}^a)^2+(\psi_{\pm n}^a)^2]} \end{aligned} \quad (10)$$

where $\psi_{\pm n}^a$ is the phase shift of the $\pm n^{th}$ laser FMS component traveling through the $(q \pm n)^{th}$ cavity mode within the analyte target gas at a certain frequency shift, given by $\pi\varsigma_{\pm n}^a/\nu_{FSR}^{0,Lock}$.

2.4. Simulations

For conventional NICE-OHMS, the laser frequency is scanned by altering the cavity length. However, ν_m is step scanned in the self-calibrated NICE-OHMS scheme, meanwhile the cavity length is automatically altered through feedback. This results in a scanned optical frequency with a nonlinear response due to gas absorbance. To illustrate and scrutinize this phenomenon, the laser frequency is simulated and analyzed as a function of ν_m. To mimic the experimental conditions (see below), the cavity length is assumed to be 39.6 cm while the finesse is taken as 1.42×10^5. The modulation index β is set to 1.2 and the scanning range of the modulation frequency ν_m is from 378.516 MHz to 378.521 MHz.

Figure 3 depicts a simulation of the laser frequency as a function of ν_m under a set of conditions. The red dashed line in each upper window of the panels corresponds to the laser frequency response under the condition of $\alpha_0 L_0 = 0$. In those cases, ν_0^l is simply given by $q\nu_m$. The black solid curves in the upper windows of the panels (a) - (c) represent the laser frequency responses for three different intracavity absorbance, *viz.* $\alpha_0 L_0 = 0.2\ \pi/F$, $0.4\ \pi/F$, and $0.6\ \pi/F$, respectively, simulated by solving the Eqs. (5)–(8) with the given values of β, and $\alpha_0 L_0$ and the given expressions for $\chi_{q\pm n}^{c,r,a}$ and $\bar{\chi}_{q\pm n}^{a,disp}$. In addition, the ν_0^l, $\nu_{FSR}^{0,Lock}$and the relative frequency deviation for the $\pm n^{th}$ laser FMS components $\varsigma_{\pm n}^a$, are obtained during this solving process, while the value of q is taken as the ratio of the transition center frequency to the FSR of an empty cavity.

The lower window in each panel shows the corresponding deviations of the laser frequency $\Delta\nu_0^l$ due to the presence of the absorber (i.e., the difference between the two curves in the upper windows, with and without absorber in the cavity). As can be seen, the lineshape of $\Delta\nu_0^l$ shows an asymmetrical profile that originates from the nonlinear laser frequency scan whose magnitude increases with $\alpha_0 L_0$. This is the basis for the self-calibration feature of the presented NICE-OHMS methodology.

Based on the Eqs. (9) and (10), the solved values of $\varsigma_{\pm n}^a$, the given values of F, β, and $\alpha_0 L_0$, and the given expressions of $\chi_{q\pm n}^{c,r,a}$ and $\bar{\chi}_{q\pm n}^{a,disp}$, simulations of the NICE-OHMS signals as a function of ν_m have been performed. The panels (a)–(c) in Fig. 4 show the self-calibrated Db NICE-OHMS signals at the dispersion phase for the same three intracavity absorbances as above, i.e., for $\alpha_0 L_0 = 0.2\ \pi/F$, $0.4\ \pi/F$ and $0.6\ \pi/F$, respectively. Compared to conventional

Optics EXPRESS

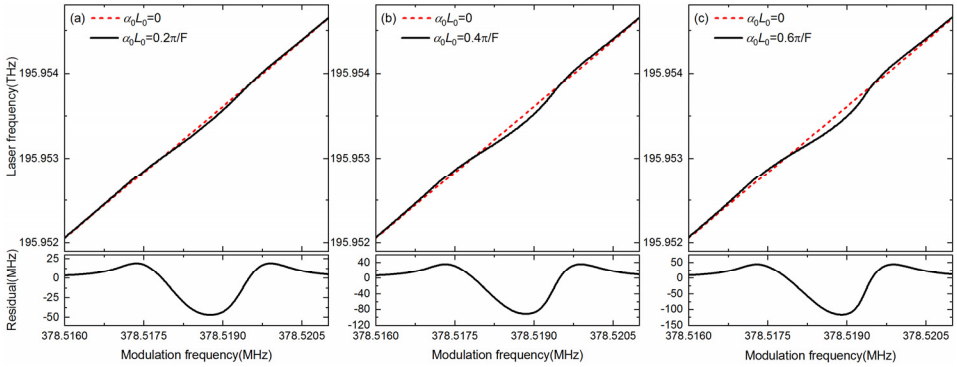

Fig. 3. The panels (a) - (c) show, by the black curves, the simulated laser frequencies as a function of ν_m under the conditions of $\alpha_0 L_0 = 0.2\ \pi/F$, $0.4\ \pi/F$ and $0.6\ \pi/F$, respectively. The red dashed line in each panel shows the simulated laser frequency for an empty cavity (i.e., for $\alpha_0 L_0 = 0$). The corresponding frequency deviations are displayed in the lower parts of the panels.

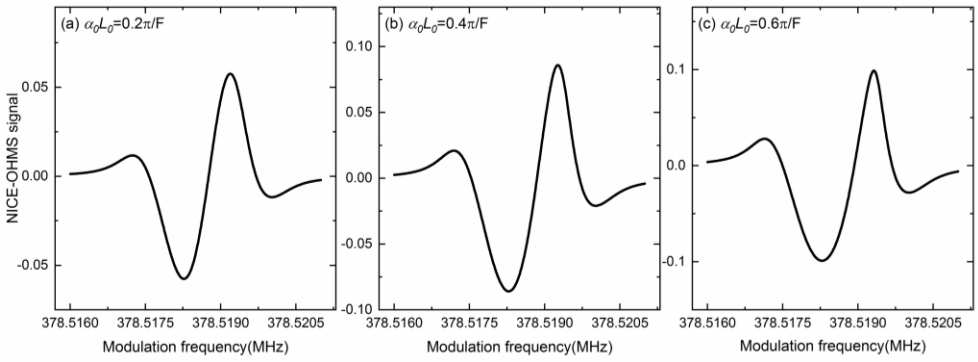

Fig. 4. The panels (a) - (c) present simulations of the self-calibrated Db NICE-OHMS signal at dispersion phase under the conditions of $\alpha_0 L_0 = 0.2\ \pi/F$, $0.4\ \pi/F$ and $0.6\ \pi/F$, respectively.

NICE-OHMS, the lineshape of this self-calibrated NICE-OHMS signal exhibits a pronounced asymmetry due to the nonlinear laser frequency response.

When conventional NICE-OHMS is applied to trace gas detection, the concentration of the gas addressed is extracted by fitting the NICE-OHMS signal to a theoretical lineshape. In order to be able to do this, the system has to be calibrated, which normally is done by addressing a series of standard concentration of gases and creating a so-called calibration curve. This is often time consuming and can be a source of uncertainty. As was noted by Schmidt et al. [19], it is alternatively possible to assess the concentration by monitoring the modulation frequency, ν_m. However, in this case, the signal often has a low SNR, which makes such assessments incompatible with high sensitivity assessments [19].

For the self-calibrated NICE-OHMS methodology, on the other hand, due to the fact that the concentration is uniquely associated to the nonlinear laser frequency response and an instrumentation factor that can be assessed at an arbitrary, but sufficiently high, gas concentration, to obtain the concentration of gas, no calibration is needed. In this case, a calibration - free assessment can be obtained by the use of high SNR NICE-OHMS signals.

Optics EXPRESS

3. Experimental setup

The self-calibrated NICE-OHMS experimental setup is illustrated in Fig. 5, which closely resembles the setup by Liu et al. [28]. We utilize an Erbium-doped fiber laser (EDFL), emitting light at a wavelength of 1530 nm, addressing the $P_e(10)$ transition of C_2H_2 at 6531.7803 cm^{-1} [29]. The laser frequency was controlled by the laser's internal PZT together with a fiber-coupled acoustic-optic modulator (f-AOM). A fiber-coupled electro-optic modulator (f-EOM), simultaneously driven by two radio frequencies ($\nu_{PDH} = 25$ MHz and $\nu_m \approx 378.520$ MHz), was used to concurrently generate the sidebands for the PDH and DVB techniques. The use of an off-axis parabolic mirror (OAP) and etalon immune distances effectively reduced unwanted interference effects [30].

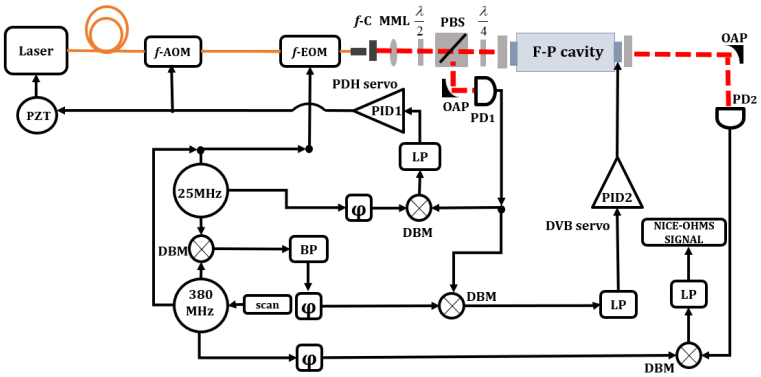

Fig. 5. Schematic diagram of the experimental setup of self-calibrated NICE-OHMS. f-C, fiber-coupled collimator; MML, mode matching lens; PBS, polarization beam splitter; φ, phase shifter; BP, band pass filter; LP, low pass filter; and DBM, doubled balance mixer.

The F-P cavity is composed of two plane-concave high-reflectivity mirrors with a reflectivity of 99.9978%, resulting in a finesse of 1.42×10^5. The spacing of the high-reflective mirrors is 39.6 cm, corresponding to FSR of 378.5 MHz.

As was alluded to above, the signal from the photodetector (PD1) is demodulated at both ν_{PDH} and ν_m-ν_{PDH} to derive the error signals for the PDH and DVB lockings, respectively. The former establishes a link between the laser frequency and the cavity mode via the homemade proportional-integral-derivative feedback loop (PID1) to the laser PZT and f-AOM. The latter correlates the modulation frequency to the FSR through a second feedback loop (PID2) to the cavity PZT. By synchronizing the two locking systems, the laser frequency is coupled to the modulation frequency whereby the detuning of the laser frequency can be accurately controlled by scanning of the latter (i.e., ν_m). The signal from PD2 is demodulated at ν_m, resulting in the NICE-OHMS signal.

4. Experimental results

To verify the theory presented in Section 2, the $P_e(10)$ transition of C_2H_2 was addressed. Measurements were performed at $\alpha_0 L_0 = 0.019$ π/F, 0.041 π/F, 0.077 π/F, 0.276 π/F, 0.423 π/F and 0.589 π/F, for which the partial pressures of C_2H_2 at the target transition were 2, 4.2, 7.8, 28, 43 and 60 μTorr, respectively. The laser frequency was scanned by stepping the modulation frequency ν_m with steps of 10 Hz. Figure 6 presents the self-calibrated Db NICE-OHMS signals at the dispersion phase from 100 ppm of C_2H_2 under a variety of total pressures: 20 mTorr [Fig. 6(a), partial pressure of 2 μTorr], 42 mTorr [Fig. 6(b), partial pressure of 4.2 μTorr], 78 mTorr [Fig. 6(c), partial pressure of 7.8 μTorr], 280 mTorr [Fig. 6(d), partial pressure of 28 μTorr],

Optics EXPRESS

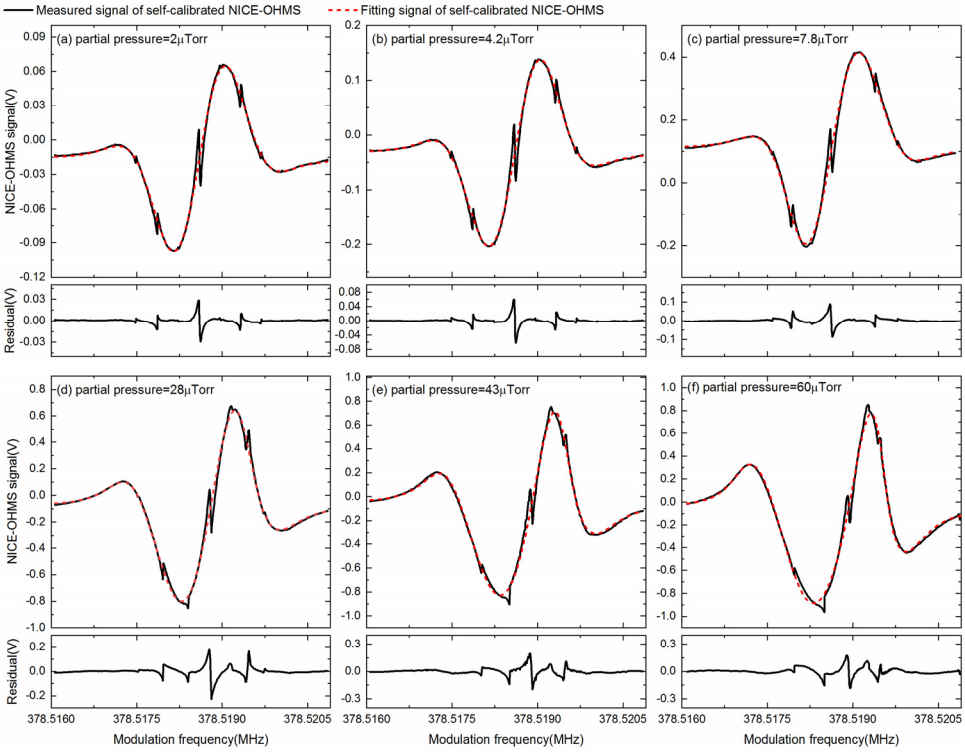

Fig. 6. The panel (a) - (f) display the measured signals of self-calibrated NICE-OHMS at dispersion phase (black curves) together with theoretical fits (red dashed curves) for partial pressures of C_2H_2 of 2, 4.2, 7.8, 28, 43 and 60 μTorr. The black curves in the lower windows of each panel show the fitting residuals.

430 mTorr [Fig. 6(e), partial pressure of 43 μTorr], and 600 mTorr [Fig. 6(f), partial pressure of 60 μTorr]. Since the total pressure is significantly less than 1 Torr, the lineshape is dominated by Doppler broadening, and the signal amplitude only depends on the partial pressure that represents the concentration of the target gas. In the figure, the experimental data is represented by the black solid curves in the upper windows of each panel, while the red dashed curves correspond to the fits obtained using the previously established theoretical model. Each lower window in the various panels shows the corresponding residual of the fit. Since the residuals are relatively flat overall (with the exception of the sub-Doppler features that are not taken into account by the fitting model), the overall congruence of the theoretical and experimental lineshapes is satisfactory.

To assess the ability of the system to measure gas concentration, the fitted partial pressures and the fitted instrument factor η(V) are shown, as a function of given partial pressure, by the black squares in the upper windows of Figs. 7(a) and (b), respectively. The red solid curve in the upper window in Fig. 7(a) shows the function of 'y = x'. The relative errors of the fitted partial pressures (with respect to the given ones), which refers to the ratio of the difference between the fitted partial pressure and the given partial pressure to the given partial pressure, are shown by the black squares in the lower window of the same panel. The data show that the relative errors are from -7.6% to +23%. As seen in the lower window of Fig. 7(b), the relative errors of the fitted instrument factor η is close to zero for higher partial pressures while they gradually increase for smaller partial pressures. This implies that η tends to a constant value when the partial pressure increases (in this case, beyond 7.8 μTorr). The reason for the larger variation at lower partial pressures is attributed to the fact that the nonlinear response of the laser frequency

Optics EXPRESS

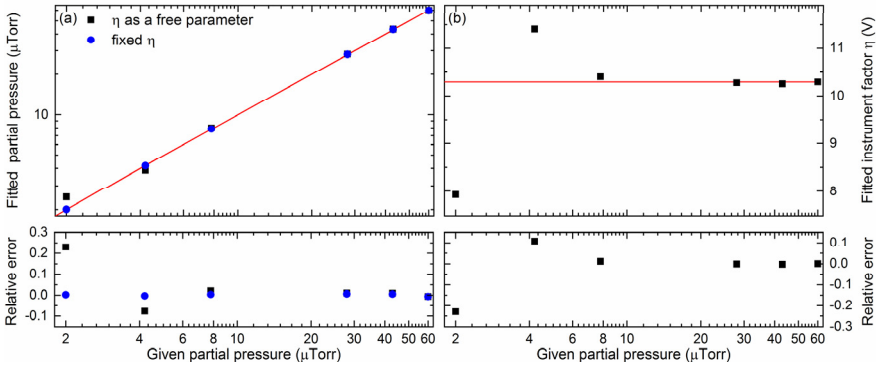

Fig. 7. The fitted partial pressure (black squares in panel (a)) and fitted instrument factor η (black squares in panel (b)) as a function of given partial pressure (fitted partial pressure and η both as free parameter) and the corresponding relative error ((black squares in each lower panel). Panel (a) shows the fitted partial pressure with a fixed η (blue dots) and the corresponding relative error (blue dots in the lower panel). The red line in panel (a) displays a dependency of 'y = x' and the red line in panel (b) shows a line of 'y = 10.29'.

becomes weaker (whereby the contribution of the laser frequency to the fit becomes smaller) when the absorption amplitude decreases.

It was found that, for the particular transition addressed in this work, and with the settings of the instrument used, the fitted value of η approaches 10.29 for higher partial pressures (up to 60 μTorr). Using this value of η as a fixed value in the fits for the lower partial pressures, which are shown by the blue dots in panel (a) of Fig. 7, produces smaller relative errors than if η was treated as a free parameter. This implies that it is advisory to set the η parameter to the value it takes at high partial pressures (high SNRs conditions). The relative error of the fitted partial pressure with fixed η is shown to be limited to 0.65% in the lower panel in Fig. 7(a). The results verify the application effectiveness of the self-calibrated NICE-OHMS to trace gas detection.

5. Conclusion

The ability to accurately determine gas concentrations in the ppt or lower level is crucial in many fields, such as for traceable quantification of radiocarbon ^{14}C for carbon emission. In this paper, we introduce a self-calibrated NICE-OHMS technique that eliminates the need for external calibration. This is accomplished by switching the feedback target of the DeVoe-Brewer (DVB) locking procedure from the FMS modulation frequency to the cavity length.

We establish a theoretical model of the self-calibrated NICE-OHMS for an arbitrary modulation index by analyzing the shift of cavity modes caused by intracavity absorption, the PDH and DVB locking processes, and the generation mechanism of NICE-OHMS signal. Our theory indicates that gas absorption information can be encoded in the laser frequency and NICE-OHMS signal, resulting in an asymmetric signal lineshape whose form and size can be used to unambiguously assess the gas concentration.

To experimentally verify the self-calibrated NICE-OHMS methodology, we build a setup and measure a series of dispersion signals under different levels of absorbance. We find that the obtained self-calibrated dispersion signals fit well with the theoretical model, with only the instrument factor (η) and partial pressure as free parameters for the C_2H_2 partial pressures of 2, 4.2, 7.8, 28, 43, and 60 μTorr. Since the η parameter comprises, among other things, the integrated linestrength of the transition, it takes a unique value for each transition addressed. It needs therefore to be assessed once for each transition addressed. For higher partial pressures (in

Optics EXPRESS

this work, above 7.8 μTorr), the η tends to a constant value and the technique exhibits excellent calibration-free capabilities. Since the relative error of the fitted η gradually increases as the partial pressure decreases, the value of the η parameter should be assessed at a pressure for which the SNR is adequate and then be used as a fixed parameter. To retrieve an accurate partial pressure also for small absorption, η should be set to the value it achieves when fitted to the self-calibrated dispersion signal at a larger partial pressure (in this work, larger than 7.8 μTorr). This approach can determine the partial pressures free of calibration with a relative error to 0.65% which is superior to the concentration accuracy with the existing gas distribution methods.

For an absorption system dominated by Doppler broadening, the upper pressure limit is around 0.1 atm. If this pressure is applied, the concentration will be 260 ppb for a partial pressure of 2 μTorr. Under this situation, the SNR (1σ) of the measured signal is around 600 according to the Fig. 6(a). The MDC of 430 ppt can be derived, corresponds to an integrated absorption of 2.62×10^{-11} cm^{-1}. By further improving the locking performance, higher sensitivity could be achieved. Overall, the instrument factor η determined by the fitting process make the NICE-OHMS free of calibration, the highly sensitive detection capability of NICE-OHMS is still maintained. Therefore, the self-calibrated NICE-OHMS technique offers a reliable and efficient method for calibration-free ultra-sensitive gas detection.

Funding. National Key Research and Development Program of China (2022YFC3700329); National Natural Science Foundation of China (61905134, 61905136, 62175139); Program for the Scientific Activities of Selected Returned Overseas Professionals in Shanxi Province (20220001); Scientific and Technological Innovation Programs of Higher Education Institutions in Shanxi (2019L0062).

Acknowledgment. Yueting Zhou: writing – original draft, validation, methodology, software. Weiguang Ma: conceptualization, writing – review and editing, funding acquisition. Gang Zhao: conceptualization, validation, funding acquisition. Zihao Zhang: investigation. Yanke Li: investigation. Xiaobin Zhou: investigation, validation. Bofeng Zhang: investigation, validation. Kang Jiao: investigation, validation. Xiaojuan Yan: investigation. Chuanliang Li: resources. O. Axner: review and editing.

Disclosures. The authors declare that there are no conflicts of interest related to this article.

Data availability. The data of this study are currently not accessible to the public. However, interested individuals may obtain access to the data by contacting the authors and submitting a reasonable request.

References

1. J. L. Jimenez, G. J. McRae, D. D. Nelson, M. S. Zahniser, and C. E. Kolb, "Remote Sensing of NO and NO2 Emissions from Heavy-Duty Diesel Trucks Using Tunable Diode Lasers," Environ. Sci. Technol. **34**(12), 2380–2387 (2000).
2. G. B. Rieker, J. B. Jeffries, R. K. Hanson, T. Mathur, M. R. Gruber, and C. D. Carter, "Diode laser-based detection of combustor instabilities with application to a scramjet engine," Proc. Combust. Inst. **32**(1), 831–838 (2009).
3. M. Azhar, J. Mandon, A. H. Neerincx, Z. Liu, J. Mink, P. J. F. M. Merkus, S. M. Cristescu, and F. J. M. Harren, "A widely tunable, near-infrared laser-based trace gas sensor for hydrogen cyanide (HCN) detection in exhaled breath," Appl. Phys. B **123**(11), 268 (2017).
4. A. J. Fleisher, D. A. Long, Q. Liu, L. Gameson, and J. T. Hodges, "Optical measurement of radiocarbon below unity fraction modern by linear absorption spectroscopy," J. Phys. Chem. Lett. **8**(18), 4550–4556 (2017).
5. D. C. Meier, K. D. Benkstein, W. S. Hurst, and P. M. Chu, "Fourier Transform Infrared Absorption Spectroscopy for Quantitative Analysis of Gas Mixtures at Low Temperatures for Homeland Security Applications," J. Test. Eval. **45**(3), 20150382 (2017).
6. C. R. Webster, P. R. Mahaffy, and S. K. Atreya, *et al.*, "Mars methane detection and variability at Gale crater," Science **347**(6220), 415–417 (2015).
7. S. Mauger, J. Millen, and M. P. A. Jones, "Spectroscopy of strontium Rydberg states using electromagnetically induced transparency," J. Phys. B: At., Mol. Opt. Phys. **40**(22), F319–F325 (2007).
8. P. Kluczynski, J. Gustafsson, ÅM Lindberg, and O. Axner, "Wavelength modulation absorption spectrometry — an extensive scrutiny of the generation of signals," Spectrochim. Acta, Part B **56**(8), 1277–1354 (2001).
9. G. C. Bjorklund, M. D. Levenson, W. Lenth, and C. Ortiz, "Frequency modulation (FM) spectroscopy," Appl. Phys. B **32**(3), 145–152 (1983).
10. J. Morville, S. Kassi, M. Chenevier, and D. Romanini, "Fast, low-noise, mode-by-mode, cavity-enhanced absorption spectroscopy by diode-laser self-locking," Appl. Phys. B **80**(8), 1027–1038 (2005).
11. P. Gorrotxategi-Carbajo, E. Fasci, I. Ventrillard, M. Carras, G. Maisons, and D. Romanini, "Optical-feedback cavity-enhanced absorption spectroscopy with a quantum-cascade laser yields the lowest formaldehyde detection limit," Appl. Phys. B **110**(3), 309–314 (2013).

Optics EXPRESS

12. B. A. Paldus and A. A. Kachanov, "An historical overview of cavity-enhanced methods," Can. J. Phys. **83**(10), 975–999 (2005).
13. J. B. Paul, L. Lapson, and J. G. Anderson, "Ultrasensitive absorption spectroscopy with a high-finesse optical cavity and off-axis alignment," Appl. Opt. **40**(27), 4904–4910 (2001).
14. D. S. Baer, J. B. Paul, M. Gupta, and A. O'Keefe, "Sensitive absorption measurements in the near-infrared region using off-axis integrated-cavity-output spectroscopy," Appl. Phys. B **75**(2-3), 261–265 (2002).
15. O. Axner, P. Ehlers, A. Foltynowicz, I. Silander, and J. Wang, "NICE-OHMS – frequency modulation cavity-enhanced spectroscopy: principles and performance," *Cavity-Enhanced Spectroscopy and Sensing* (Springer Berlin/Heidelberg, 2014), pp. 211–251.
16. J. Ye, L.-S. Ma, and J. L. Hall, "Sub-Doppler optical frequency reference at 1064 μm by means of ultrasensitive cavity-enhanced frequency modulation spectroscopy of a C_2HD overtone transition," Opt. Lett. **21**(13), 1000–1002 (1996).
17. G. Zhao, T. Hausmaninger, W. Ma, and O. Axner, "Shot-noise-limited Doppler-broadened noise-immune cavity-enhanced optical heterodyne molecular spectrometry," Opt. Lett. **43**(4), 715–718 (2018).
18. H. Li, G. B. Rieker, X. Liu, J. B. Jeffries, and R. K. Hanson, "Extension of wavelength-modulation spectroscopy to large modulation depth for diode laser absorption measurements in high-pressure gases," Appl. Opt. **45**(5), 1052–1061 (2006).
19. F. M. Schmidt, W. Ma, A. Foltynowicz, and O. Axner, "Highly sensitive dispersion spectroscopy by probing the free spectral range of an optical cavity using dual-frequency modulation," Appl. Phys. B **101**(3), 497–509 (2010).
20. Y. Zhou, G. Zhao, J. Liu, X. Yan, Z. Li, W. Ma, and S. Jia, "Generation of stable and tunable optical frequency linked to a radio frequency by use of a high finesse cavity and its application in absorption spectroscopy," Chin. Phys. B **31**(6), 064206 (2022).
21. W. Ma, I. Silander, T. Hausmaninger, and O. Axner, "Doppler-broadened NICE-OHMS beyond the cavity-limited weak absorption condition – I. Theoretical description," J. Quant. Spectrosc. Radiat. Transfer **168**, 217–244 (2016).
22. R. de L. Kronig, "On the Theory of Dispersion of X-Rays," J. Opt. Soc. Am. **12**(6), 547–557 (1926).
23. H. A. Kramers, "La diffusion de la lumiere par les atomes," in *Atti Cong. Intern. Fisica (Transactions of Volta Centenary Congress) Como* (1927), pp. 545–557.
24. R. W. P. Drever, J. L. Hall, F. V. Kowalski, J. Hough, G. M. Ford, A. J. Munley, and H. Ward, "Laser phase and frequency stabilization using an optical resonator," Appl. Phys. B **31**(2), 97–105 (1983).
25. R. G. DeVoe and R. G. Brewer, "Laser-frequency division and stabilization," Phys. Rev. A **30**(5), 2827–2829 (1984).
26. P. Ehlers, J. Wang, I. Silander, and O. Axner, "Doppler broadened NICE-OHMS beyond the triplet formalism: assessment of optimum modulation index," J. Opt. Soc. Am. B **31**(7), 1499–1507 (2014).
27. P. Ehlers, I. Silander, and O. Axner, "Doppler broadened noise-immune cavity-enhanced optical heterodyne molecular spectrometry: optimum modulation and demodulation conditions, cavity length, and modulation order," J. Opt. Soc. Am. B **31**(9), 2051–2060 (2014).
28. J. Liu, G. Zhao, W. Ma, and O. Axner, "Development of a Doppler-broadened NICE-OHMS system for trace gas detection based on a single sideband phase modulator," Opt. Express **29**(26), 42411–42419 (2021).
29. I. E. Gordon, L. S. Rothman, and C. Hill, *et al.*, "The HITRAN2016 molecular spectroscopic database," J. Quant. Spectrosc. Radiat. Transfer **203**, 3–69 (2017).
30. P. Ehlers, A. C. Johansson, I. Silander, A. Foltynowicz, and O. Axner, "Use of etalon-immune distances to reduce the influence of background signals in frequency-modulation spectroscopy and noise-immune cavity-enhanced optical heterodyne molecular spectroscopy," J. Opt. Soc. Am. B **31**(12), 2938–2945 (2014).